

Curacautín ignimbrite sample collection

The Curacautín eruption produced extensive ignimbrite deposits radially around the present-day volcano and as far west as the city of Temuco (Naranjo and Moreno, 1991). The Curacautín ignimbrite (Ci) is an unconsolidated coarse ash to fine lapilli tuff of basaltic andesite composition that erupted ~12.6 ka (Marshall et al., 2022). The samples used for this study were collected by Marshall et al. (2022) during three field campaigns from 2016–2020 from exposures to the north, east, and west of Llama (Fig. S1). While Naranjo and Moreno (1991) state deposits are found up to 100 km from source, we were only able to find reliable exposures up to 30 km from the present-day vent.

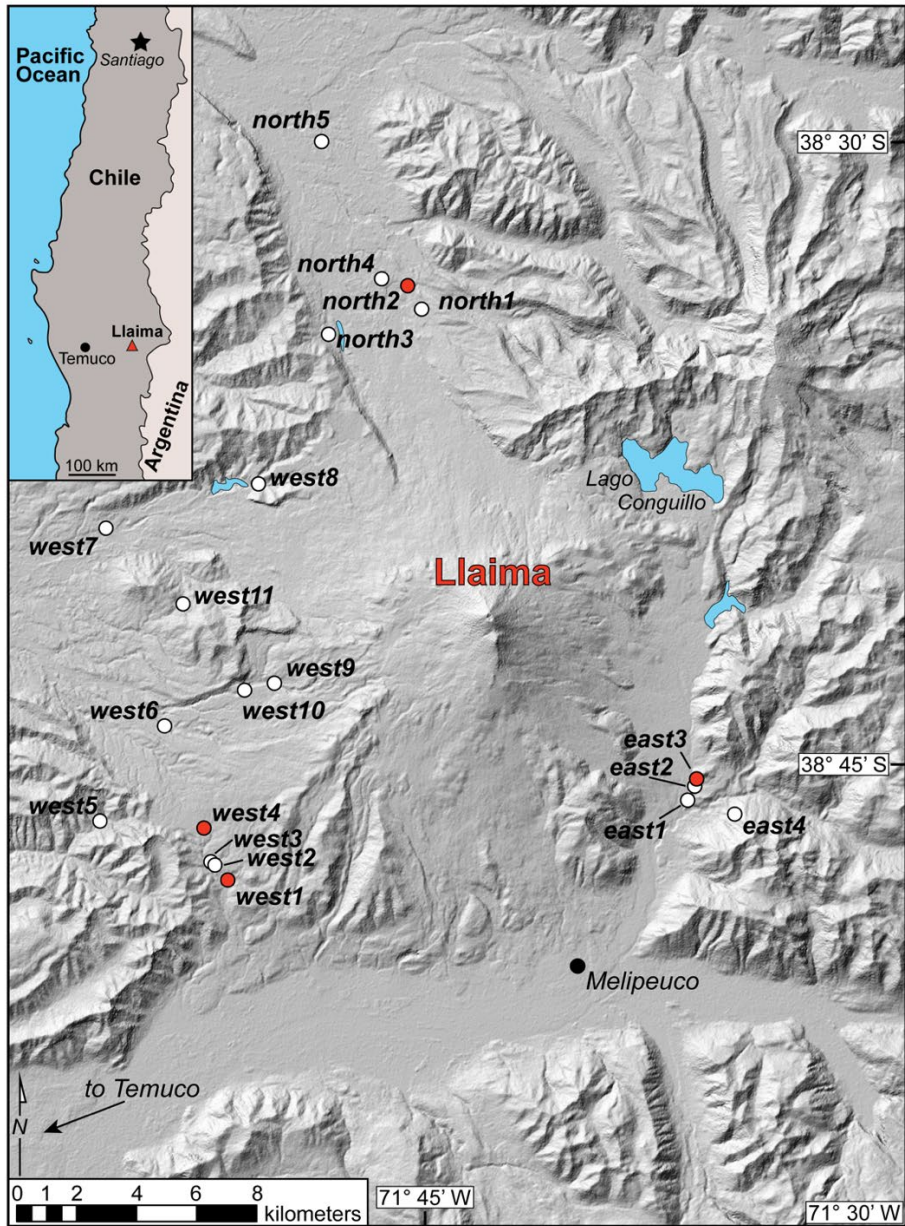


Figure S1. Sample locations from Marshall et al. (2022) (their Fig. 2) for reference with Table S1. Red symbols show locations contained charcoal for ¹⁴C dating.

Marshall et al. (2022) determined that the Ci consists of four flow units of variable thicknesses. However, identifiable contacts are poorly preserved or not present in most exposures. The best exposure of the flow units is the east side of Llaima (east1, east2, and east3 in Fig. S1); however, the base of the stratigraphically lowest unit is not exposed (Fig. S2). Bulk samples consisting of juvenile ash, lapilli, blocks, and country rock lithics were collected from the eastern stratigraphic section at regular intervals and from other fresh exposures identified around Llaima; charcoal for ^{14}C dating was collected where present (Fig. S1). Ash and lapilli were sieved for granulometric analysis. Up to 100 lapilli-sized pyroclasts were measured for density following the methods of Houghton and Wilson (1989). Componentry was counted for the eastern stratigraphic section down to 1 ϕ .

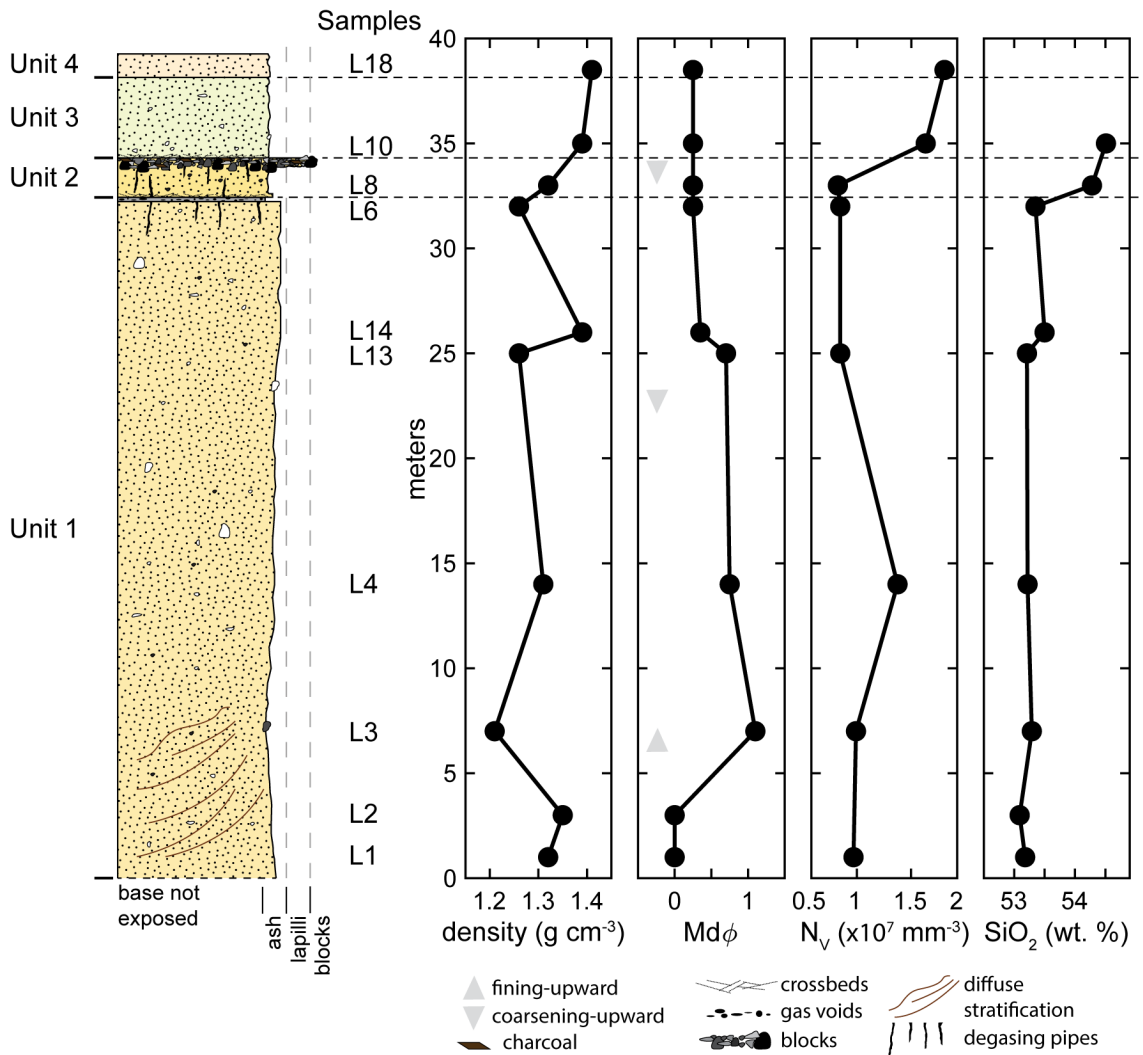


Figure S2. Eastern stratigraphic section reported in Marshall et al. (2022) (their Fig. 4) alongside density, Mdφ, volumetric microlite number densities (N_v), and SiO₂-content. The stratigraphic column is constructed from samples across exposures east1, east2, and east3 (Fig. S1).

Samples investigated in this study (Table S1) were collected from fresh exposures at various distances from the present-day vent and throughout the four flow units exposed in the

eastern outcrops. Lapilli-sized pyroclasts representing the average density and \pm one standard deviation were selected for scanning electron microscopy and x-ray tomography.

Clasts selected for scanning electron microscopy (SEM) and x-ray computed microtomography (μ CT) were selected based on clast density. SEM images were collected on a Teneo FEI Scanning Electron Microscope at the Boise State University Center for Materials Characterization. Imaging beam current was 6.4 nA and the beam current accelerating voltage was 15 kV. Clast cores 3.3 mm in diameter from the center of clasts were drilled for μ CT and imaged at Lawrence Berkeley National Laboratory's Advanced Light Source on beamline 8.3.2 using 25–30 kV monochromatic X-rays, 200 ms exposure times, a PCO edge camera with 5X Mitutoyo lens, and a 50 mm LuAG scintillator. Samples were imaged during 180° continuous sample rotation. The linear voxel size of images is 1.3 μ m.

We observed heterogeneous domains of vesicle textures in all size ranges of Ci pyroclasts across all exposures, in 85% of our thin sections, and in 53% of our tomography datasets. Entrained lithics exist in 92% of all thin sections and tomography datasets and in every block-size hand sample we collected. We attribute the lower percentage of tomography datasets containing heterogeneous domains of vesicle textures with the small diameter of cores collected (3.4 mm), which reduces the possibility of intersecting such domains. Additionally, at the time tomography data were collected, the fusing hypothesis presented in this manuscript was not a concept we were investigating and thus was not factored in to how we collected those data.

Table S1. Location information for images in manuscript figures.

Figure	Sample	Unit ^a	Outcrop name ^b	Height above base ^c of unit (m)	Distance from vent ^c (km)
1A	L25	unk	west4	1	16.5
1B	L9	Unit 2	east3	1.5	12
1C	L42	unk	west1	0.1	16.5
1D	L42	unk	west1	0.1	16.5
1E	L23	unk	west9	0.5	10
2A	L10	Unit 3	east3	0.1	12
2B	L21	unk	east4	0.1	13
2C	L25	unk	west4	0.1	16.5
2D	L2	Unit1	east1	3	12
2E	L4	Unit1	east2	14	12
2F	L6	Unit 1	east3	32	12
2G	L3	Unit 1	east1	7	12
2H	L3	Unit 1	east1	7	12
2I	L2	Unit 1	east1	3	12
4E ^d	L4	Unit 1	east2	14	12
4F	L3	Unit 1	east1	7	12
4G	L25	unk	west4	0.1	16.5
4H	L34	unk	north2	0.5	15

^{a,b}Unit and outcrop names from Marshall et al. (2022). See Figure S1.

^cIn most cases, the base of the deposit is not exposed, and base here refers to the lowest-most point of the exposure

^dValdivia et al. (2022)

^eMeasured in GoogleEarth

Ci crystal size distributions

Plagioclase crystal size distributions (CSDs) were measured and reported in Valdivia et al. (2022) (Fig. S3). Those authors manually traced plagioclase microlites using backscattered electron images collected on a Teneo FEI Field Emission Scanning Electron Microscope at the Boise State University Center for Materials Characterization using a beam current of 6.4 nA and 15 kV accelerating voltage at 1500–2000X magnifications. Microlites were assigned a crystal habit using *CSDslice* v.5 (Morgan and Jerram, 2006) and used as inputs for *CSDcorrections* v.1.6 (Higgins, 2000) to create plagioclase CSDs. Using linear regression fitting, Valdivia et al. (2022) fit two segment regressions with high R^2 values (Fig. S3) to the CSDs, and using CSD theory and, following the methods of Bamber et al. (2020), calculated timescales of crystallization of seconds to hours. Due to the difficulty in identifying units outside of the eastern stratigraphic section, the CSD samples are all from the eastern stratigraphic sequence (Figs. S1, S2).

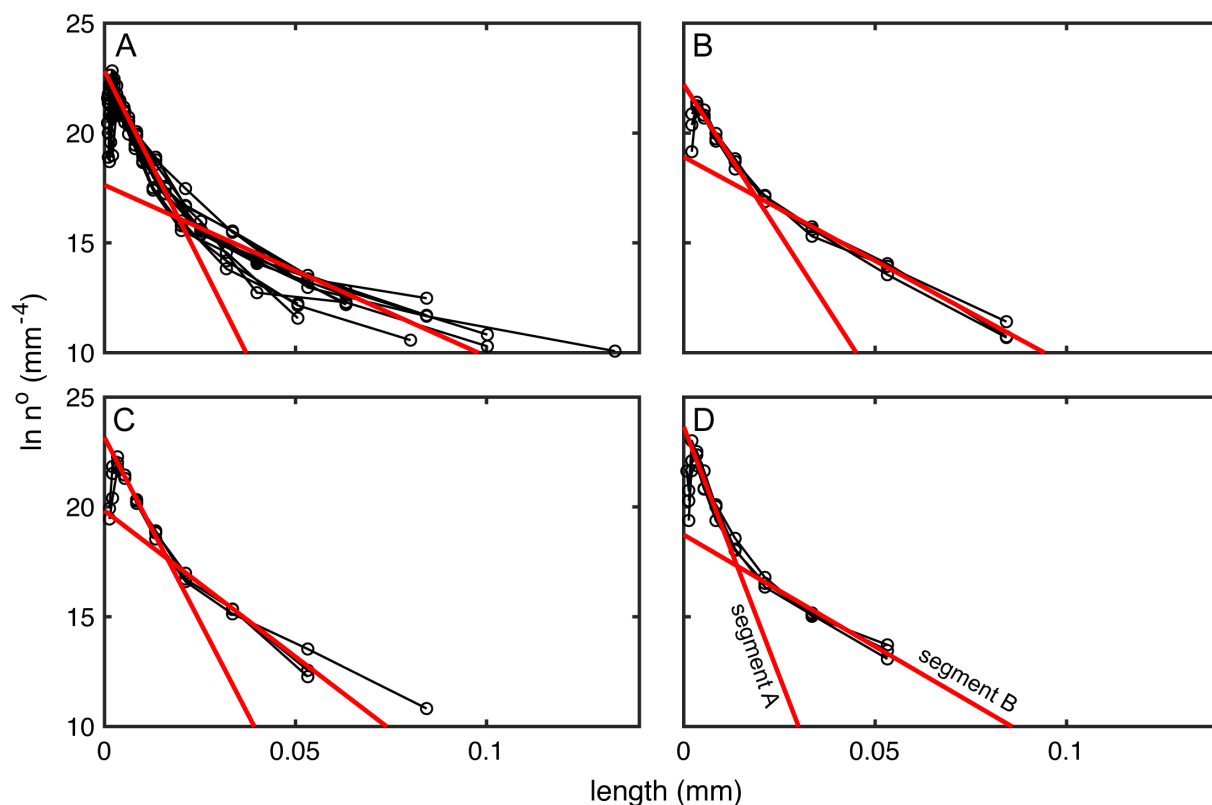


Figure S3. Crystal size distributions (CSDs) with fit regressions based on R^2 values from Valdivia et al. (2022) (their Fig. 4). A) Unit 1. A total of three thin sections were analyzed, one each for the bottom, middle, and top of the unit. B) Unit 2. C) Unit 3. D) Unit 4. Segment A regressions represent late crystallization of smaller microlites whereas segment B regressions are fit to larger crystals produced earlier in ascent. Valdivia et al. (2022) interpret this difference in regression slope as changes in ascent rate of the Curacautín magma prior to eruption.

Table S2. Samples investigated by Valdivia et al. (2022) for plagioclase crystal size distribution analysis. Refer to Figs. S1 and S2 for sample locations. Here, regressions are fit to microlite size populations with long axes (l) $>10\text{ }\mu\text{m}$ and $l\leq 10\text{ }\mu\text{m}$ (Fig 3). We calculated Pearson coefficients (ρ) for each regression fit. Each CSD is an average of 3 analyzed images; therefore, the value of ρ provided is the average of that total dataset.

Sample	Unit	Outcrop name	Number of images analyzed for CSDs	$l > 10\text{ }\mu\text{m}$ regression ρ	$l \leq 10\text{ }\mu\text{m}$ regression ρ
L18	4	east3	3	-0.978	-0.987
L10	3	east3	3	-0.989	-0.999
L8	2	east3	3	-0.990	-0.993
L6	1 (top)	east3	3	-0.951	-0.965
L4	1 (middle)	east1	3	-0.975	-0.997
L1	1 (bottom)	east1	3	-0.956	-0.997

$$^a \rho = \frac{n\sum xy - \sum x \sum y}{\sqrt{[n\sum x^2 - (\sum x)^2][n\sum y^2 - (\sum y)^2]}} \text{ where } n = \text{number of CSD points}$$

References Cited

- Bamber, E.C., Arzilli, F., Polacci, M., Hartley, M.E., Fellowes, J., Di Genova, D., Chavarria, D., Saballos, J.A., and Burton, M.R., 2020, Pre- and *syn*-eruptive conditions of a basaltic Plinian eruption at Masaya Volcano, Nicaragua: The Masaya Triple Layer (2.1 ka): Journal of Volcanology and Geothermal Research, v. 392, p. 1–16, doi: 10.1016/j.jvolgeores.2019.106761.
- Higgins, M.D., 2000, Measurement of crystal size distributions: American Mineralogist, v. 85, p. 1105–1116.
- Houghton, B.F., and Wilson, C.J.N., 1989, A vesicularity index for pyroclastic deposits: Bulletin of Volcanology, v. 51, p. 451–462, doi: 10.1007/BF01078811.
- Marshall, A.A., Brand, B.D., Martínez, V., Bowers, J.M., Wanless, V.D., Andrews, B.J., Manga, M., Valdivia, P., and Giordano, G., 2022, The mafic Curacautín ignimbrite of Llaima volcano, Chile: Journal of Volcanology and Geothermal Research, v. 421, no. 107418, doi: 10.1016/j.jvolgeores.2021.107418.
- Morgan, D.J., and Jerram, D.A., 2006, On estimating crystal shape for crystal size distribution analysis: Journal of Volcanology and Geothermal Research, v. 154, p. 1–7, doi: 10.1016/j.jvolgeores.2005.09.016.
- Naranjo, J.A., and Moreno, H., 1991, Actividad explosiva postglacial en el volcan Llaima, Andes del sur (38°45'S): Revista Geológica de Chile, v. 18, no. 1, p. 69–80.
- Valdivia, P., Marshall, A.A., Brand, B.D., and Manga, M., 2022, Mafic explosive volcanism at Llaima volcano: 3D X-ray microtomography reconstruction of pyroclasts to constrain shallow conduit processes: Bulletin of Volcanology, v. 84, no. 2., doi: 10.1007/s00445-021-01514-8.